Trapping and release of impurities in TiN: A first-principles study

L. Tsetseris
Department of Physics, Aristotle University of Thessaloniki, GR-54124 Thessaloniki, Greece and Department of Physics and Astronomy, Vanderbilt University, Nashville, Tennessee 37235, USA

N. Kalfagiannis and S. Logothetidis
Department of Physics, Aristotle University of Thessaloniki, GR-54124 Thessaloniki, Greece

S. T. Pantelides
Department of Physics and Astronomy, Vanderbilt University, Nashville, Tennessee 37235, USA and Oak Ridge National Laboratory, Oak Ridge, Tennessee 37831, USA
(Received 16 April 2008; revised manuscript received 29 July 2008; published 24 September 2008)

Films of titanium nitride, a prototype refractory material, typically contain a sizeable amount of impurities that are known to affect the properties of the host crystal. Here, we use first-principles calculations to identify the atomic-scale mechanisms that control the presence of the most common impurities (O, H, C, Ar, and He) in TiN. We identify the role of N vacancy sites as very efficient trapping centers, but we also show that the interaction between trapped species and N interstitials can lead either to impurity release or the formation of stable defect complexes. The results explain the fundamentals of key processes in the preparation of TiN films such as postgrowth impurity removal through nitridation or thermal desorption. We also present results on the effect of impurities on the electronic properties of TiN and on local vibrational modes around extrinsic species. We describe the bonding topology in the vicinity of impurities using the electron localization function and we discuss the relevance of our findings for physical traits of TiN films.

DOI: 10.1103/PhysRevB.78.094111 PACS number(s): 72.80.Ga

I. INTRODUCTION

Transition-metal nitrides (TMNs) are hard refractory materials that are used in multiple types of applications[1–7] because of their renowned hardness,[4,5] excellent thermal stability,[1,2,8,9] defect impermeability,[6] and resistance to wear, oxidation, and corrosion. For example, TMN films are used as metal gates or metal gate coatings in electronic devices; while TiN, a prototype TMN system, and ZrN are also employed as decorative overlayers because of their goldlike appearance. Recently, there is a renewed interest in TMNs, following the identification of TiN-based nanocomposites as superhard materials.[10–13]

The quality of TMN films can vary significantly depending on the particular choice of one of the many available growth techniques. There is, however, a feature that is present in all growth processes: extrinsic species are always trapped in TMN films. Such species are often used intentionally, for example Ar ions[1,14,15] in physical vapor deposition and carbon[16–22] or hydrogen[16,19,20,23] in metal-organic chemical vapor deposition. In other cases, it is simply impossible to eliminate completely impurities such as oxygen.[24–30] In general, nonequilibrium conditions during growth, for example the use of highly energetic Ar ions for sputtering, can facilitate trapping of extrinsic species.

The presence of defects has a dual significance for typical TMN-based applications. The defects modify the physical properties of the TMN samples, leading to changes in their residual stress,[1,14] resistivity,[24,26–28] and color.[29,30] In addition, trapped species such as hydrogen or oxygen may be released at a later stage, and the released impurities can trigger new processes either in the TMN regions or in other materials in the vicinity.[11,31,32] Thermal desorption[33] of trapped inert gas atoms has also been employed to study the diffusion of native defects in TMNs. Even though the importance of impurities for transition-metal compounds is well established experimentally, the atomic-scale mechanisms that control their presence in these materials remain, to our knowledge, largely unknown.

In this paper, we use first-principles calculations to study the trapping and release of the most common extrinsic species in TiN. In particular, we consider O, H, C, Ar, and He atoms in various configurations inside the rocksalt structure of δ-TiN. We find that a large amount of energy is released when these species move to occupy N vacancy sites of the host crystal. The subsequent arrival of a N interstitial or a N interstitial pair, however, changes the fundamentals of impurity incorporation and results in the selective release of trapped impurities. We describe the structural properties of the created defects and the energetics of the release process. We also find that certain impurities, for example O interstitials, have a discernible effect on the electronic properties of TiN even when found in low numbers. We conclude with a discussion on the relevance of the results for various TiN-based applications.

II. METHOD

The calculations were performed within density-functional theory with a generalized-gradient-approximation-corrected exchange-correlation functional,[34] a plane-wave basis set with an energy cutoff (E_c) of 400 eV, and projector-augmented wave potentials (PAWs) (Ref. 35) as implemented in the VASP code.[36] The results we present below on trapping and binding energies are based on $3\times3\times3$ super-

 ©2008 The American Physical Society

TABLE I. Formation energies (E_f) for O and H impurities in TiN based on Eqs. (1) and (2). Positive (negative) E_f indicates an energy gain (penalty) for the formation of the impurity configuration in TiN.

Structure	E_f (eV)	Nearest neighbor (distance)
Figure 1(a)	5.79	Ti (2.20 Å)
Figure 1(c)	−0.91	Ti (1.91 Å)
H at N vacancy	0.38	Ti (2.18 Å)
Figure 5(c)	−2.30	N (1.06 Å)

cells with 108 Ti and 108 N atoms when no defects are present. In these total-energy calculations we used the MOHNKORST-PACK scheme[37] for Brillouin-zone sampling and $3\times3\times3$ k grids. The lattice constant was fixed at 4.2366 Å.[3] The interaction energies E_i between defects were obtained by combining the energy of the host crystal and the energies of supercells with isolated defects and with defect complexes. Similar methodology was employed for extensive studies of point defects in transition-metal nitrides[8,9,38] and titanium carbide.[39] We also probed the effect of impurities on the electronic properties of TiN specifically on the electronic density of states (DOS). In this case, the calculations are more computationally intensive and we used supercells with 32 Ti and 32 N atoms in the defect-free case. In the calculation of DOS, the integration in reciprocal space was performed with the tetrahedron method.[40]

In Table I we give the formation energies (E_f) of O and H defects in various configurations. For an O interstitial defect we have

$$E_f = E_i - E^0_{\mathrm{TiN}} - \frac{1}{2}E_{\mathrm{O}_2}, \tag{1}$$

where E_i, E^0_{TiN}, and E_{O_2} are the absolute total energies of the impurity configuration, of TiN (for 108 Ti and 108 N atoms), and of an O_2 molecule, respectively. For an O atom trapped at N vacancy site we have

$$E_f = E_i - E^{N_V}_{\mathrm{TiN}} - \frac{1}{2}E_{\mathrm{O}_2}, \tag{2}$$

where $E^{N_V}_{\mathrm{TiN}}$ is the absolute total energy of a TiN cell with one N vacancy (108 Ti and 107 N atoms). In the case of H, the formation energies are calculated with the same formulas except that the energy E_{H_2} of a hydrogen molecule takes the place of E_{O_2}. Based on the above expressions, a positive (negative) E_f indicates that the formation of the impurity configuration in TiN relates to an energy gain (penalty) with respect to the reference structures.

III. RESULTS

We present below the results for trapping and release of oxygen, carbon, hydrogen, helium, and argon impurities in TiN. In each case, we discuss the details of trapping at N vacancy sites and the effect of interactions between the trapped species and one or two N interstitial atoms.

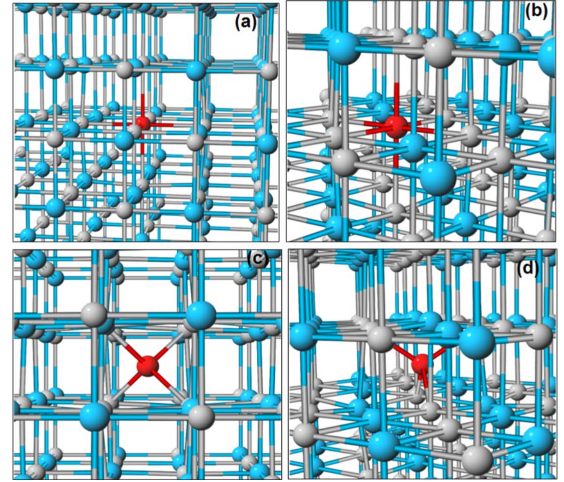

FIG. 1. (Color online) Oxygen in the rocksalt structure of δ-TiN. (a) and (b) O at a N vacancy site and (c) and (d) interstitial O in the most stable tetrahedral configuration. [Ti: light gray, N: gray (cyan), and O: dark gray (red) spheres.]

A. O impurities in TiN

The most stable configuration of an oxygen interstitial atom in TiN is the tetrahedral structure shown in Figs. 1(c) and 1(d). The O atom forms covalent bonds with the surrounding Ti atoms and pushes them outward at a distance of 1.908 Å. Other stable configurations correspond to split interstitial geometries with N-O dimers aligned along the (111) and $(10\bar{1})$ directions. These split interstitial structures are depicted for native N defects in Fig. 2 of Ref. 8. In the present case, the N-O dimer has an extended bond length of 1.37 Å. Unlike the native defect case, the split interstitial configurations of O in TiN are higher in energy compared to the tetrahedral structure, and the energy difference is 0.43 and 0.75 eV for (111) and $(10\bar{1})$ N-O dimers, respectively.

The energetics of O trapping changes completely when the oxygen atom reaches a nitrogen vacancy (V_{N}) of TiN. The interstitial oxygen atom moves then to occupy the vacancy site, releasing a large energy of 6.7 eV. In this configuration, shown in Figs. 1(a) and 1(b), the oxygen atom pushes the surrounding Ti atoms at a distance of 2.20 Å, while the backbonds of these Ti atoms to neighboring N and Ti atoms shrink to 2.05 and 2.93 Å, respectively. The energy gains associated with impurities at N vacancy sites and the binding energies of complexes between impurities and N interstitials are summarized in Table II. Even though a N vacancy is a very stable trapping site for O in TiN, this configuration proves to be metastable when a native N interstitial (I_{N}) arrives in its vicinity. In this case, an I_{N} species replaces the O atom at the vacancy, resulting in an ideal TiN network with a released O interstitial. The process is exothermic with a release of 0.31 eV energy.

The released O interstitial can interact further with other I_{N} species in TiN. We have studied an extensive number of possible pairs of an O atom with a N interstitial in TiN. The most stable such pair is shown in Figs. 2(a) and 2(b). The O atom of the pair is in a tetrahedral configuration and the extra N atom is in a $(10\bar{1})$ split-interstitial arrangement next to O.

TABLE II. Energy change ΔE following impurity-related processes in TiN. Positive (negative) ΔE indicates energy gain (penalty). $V_N(I_N)$ denotes a N vacancy (interstitial) in TiN.

Process	ΔE (eV)
O interstitial moves to V_N	6.70
O-I_N complex dissociates	−0.46
C interstitial moves to V_N	6.67
C-I_N complex dissociates	−0.67
H interstitial moves to V_N	2.68
H-I_N complex dissociates	−0.39
He interstitial moves to V_N	1.51
He-I_N complex dissociates	−0.57
Ar interstitial moves to V_N	6.37
Ar-I_N complex dissociates	−0.50

The distance between O and the N atoms of the split dimer is 2.171 Å. The complex has a binding energy of 0.46 eV against dissociation to individual O and I_N species so that O and N interstitials in TiN act as gettering centers for each other. In another stable O-I_N pair, whose binding energy is lower at 0.28 eV, the O and I_N species are again in vicinal tetrahedral and split-interstitial configurations but the distance between O and the dimer is 2.67 Å. A complex with O and I_N in vicinal (111) and $(10\bar{1})$ split-interstitial configurations, respectively, has an energy that is higher than the above pairs but it is also stable with a binding energy of 0.17 eV. The formation of all other studied O-I_N complexes with different combinations of tetrahedral and split-interstitial structures carries energy penalties that vary from 0.1 to 1.0 eV.

We now examine the effect of O impurities on the electronic properties of TiN and, in particular, on DOS. In Fig. 3 we compare the DOS of a defect-free TiN crystal and of a

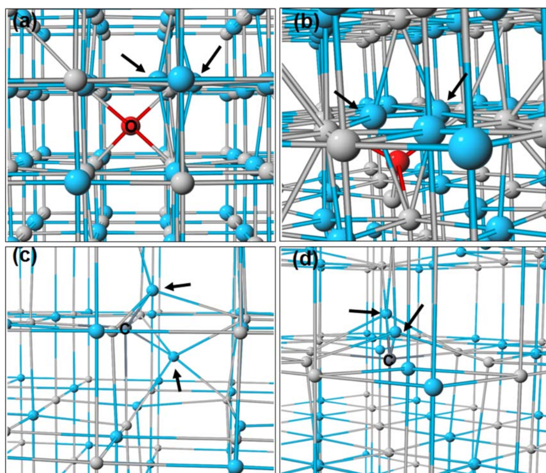

FIG. 2. (Color online) Defect complex of a N interstitial with (a) and (b) an oxygen atom and (c) and (d) a carbon atom in TiN. The arrows indicate the vicinal to O N split interstitial in (a) and (b) and the vicinal to C N interstitials in (c) and (d). [Ti: light gray, N: gray (cyan), O (red), and C: dark gray spheres.]

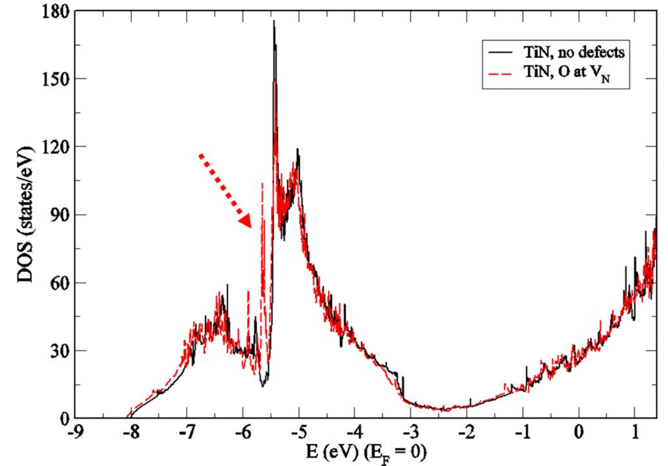

FIG. 3. (Color online) Electronic density of states and effect of oxygen atoms trapped at V_N in TiN. The results are based on supercells with 32 Ti and 32 N atoms in the defect-free case. Zero of energy is set at the Fermi level. Solid (black) line for defect-free TiN and dashed (red) line for TiN with an O atom trapped at a V_N site. The arrow shows a new peak related to the presence of O impurities.

TiN system with an O atom trapped at a N vacancy site. The results are based on $2\times2\times2$ supercells with 32 Ti and 32 N atoms in the defect-free case, and $16\times16\times16$ k grids were used for Brillouin-zone integrations. As depicted in Fig. 3, and in agreement with previous studies,[3,9] the density of states of TiN shows a valley below the Fermi level (E_F). It is centered about 2 eV below E_F and the two peaks on the left and on the right sides are dominated by the N-p bands and the Ti-d bands, respectively. The DOS comparison of Fig. 3 shows that the insertion of O at V_N sites does not alter the electronic properties of TiN significantly at least for an O concentration up to 3.125%. Nevertheless, a distinct new peak (shown with an arrow on Fig. 3) appears 5.6 eV below the Fermi level (E_F).

In the case of O interstitials, the presence of impurities has a more discernible effect on the electronic properties of TiN. In Fig. 4 we present the DOS for O interstitials in a tetrahedral structure and in a split configuration. Compared to the defect-free case of Fig. 3, we see that O split interstitials induce a broad peak (arrows 1 and 2 in the figure) in the range of 2.2–2.5 eV below E_F and isolated narrow bands (arrows 3 and 4) starting from 8.5 eV below the Fermi level. Similarly, tetrahedral O interstitials induce peaks in the DOS valley and another larger peak at bottom of the TiN valence band about 8 eV below E_F.

B. C and H impurities in TiN

The most stable configuration of a C atom in an otherwise defect-free TiN sample is shown in Figs. 5(a) and 5(b). It is the result of relaxation from an initial split-interstitial structure with a C-N dimer in the (111) direction. In the final relaxed arrangement, C occupies a site of the network and the N atom lies at a distance of 1.33 Å in the (111) direction. A split-interstitial structure with the C-N dimer along the

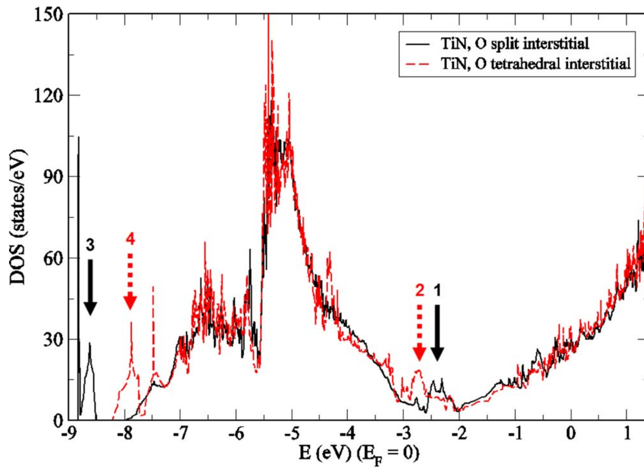

FIG. 4. (Color online) Electronic density of states and effect of interstitial oxygen atoms in TiN. The results are based on supercells with 32 Ti and 32 N atoms. Zero of energy is set at the Fermi level. Solid (black) line for an O split-interstitial structure and dashed (red) line for a tetrahedral O configuration. The arrows show peaks that are related to the presence of O impurities.

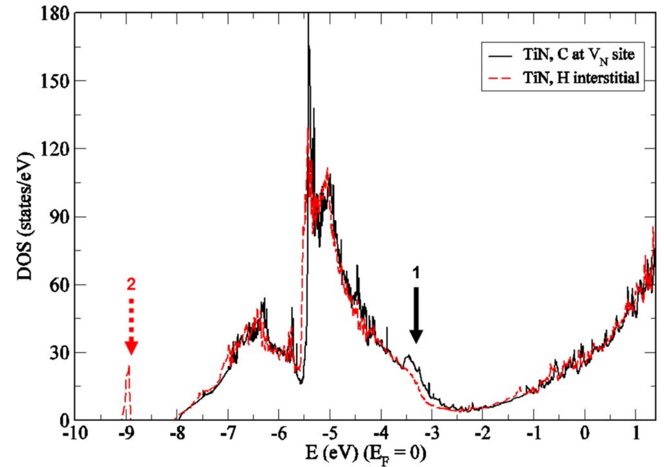

FIG. 6. (Color online) Electronic density of states and effects of trapping of carbon and hydrogen in TiN. The results are based on supercells with 32 Ti and 31 or 32 N atoms. Zero of energy is set at the Fermi level. Solid (black) line for a C atom at a V_N site and dashed (red) line for TiN with an interstitial H atom. The arrows show peaks that are related to the presence of C and H impurities.

$(10\bar{1})$ direction is higher in energy by 0.22 eV. A C interstitial in a tetrahedral position is significantly less stable by 2.19 eV. The configuration of Fig. 5(a) can be also be viewed as the trapping site of a N interstitial at a C site of TiN and the corresponding binding energy is 0.35 eV. Without the N interstitial, the structure represents a very stable configuration for C in TiN and release of C from the vacancy site would carry an energy penalty of 6.67 eV.

Similar to O interactions with N interstitials, C atoms in TiN form a number of stable complexes with I_N defects. The C-I_N complex with the lowest energy, shown in Figs. 2(c) and 2(d), comprises a C atom on a crystal site and two N atoms next to it at distances of 1.34 and 1.37 Å, respectively. The direction of both C-N bonds is close to the (111) axis and the N-C-N angle is 106°. The complex has a binding energy of 0.67 eV against dissociation to isolated C and I_N species. There are several other stable C-I_N pairs whose binding energies range from 0.5 to 0.2 eV and which contain N interstitial atoms in various split or tetrahedral configurations.

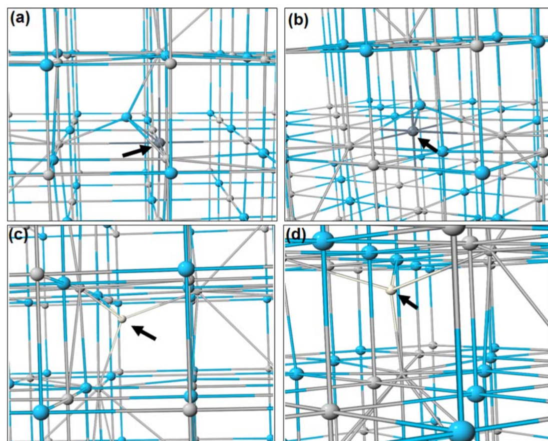

FIG. 5. (Color online) (a) and (b) C interstitial in TiN. Carbon displaces a N atom and occupies its site in the rocksalt structure. (c) and (d) H interstitial in TiN. The positions of extrinsic species are indicated with arrows. [Ti: light gray, N: gray (cyan), C: dark gray, and H: white spheres.]

Figures 5(c) and 5(d) show the lowest energy configuration for a hydrogen interstitial in TiN. It corresponds to a split interstitial in the (111) direction with a H-N dimer bond length of 1.06 Å. This configuration is marginally more stable than the tetrahedral H structure and the split configuration with a N-H dimer aligned along the $(10\bar{1})$ direction. In the former tetrahedral structure the H atom distance from neighboring Ti atoms is 1.808 Å. The energy difference between these three structures is less than 0.05 eV for the calculational parameters mentioned above. When the interstitial H atom encounters a nitrogen vacancy site it hops to V_N and the energy decreases by 2.68 eV, i.e., a N vacancy is a very stable trapping site for H in TiN. However, and similar to the above case of oxygen, the H atom can again be released to the network if a N interstitial arrives at the V_N site. The release of H is an exothermic reaction with an energy gain of 4.34 eV.

H atoms can trap N interstitials in TiN in various stable H-I_N complexes. The energy of the most stable H-I_N pair is 0.39 eV lower than the energy of isolated H and I_N species in TiN. The defect complex comprises a N split-interstitial dimer whose direction is slightly off the (111) axis, and a vicinal H atom bonded to a network N atom at a distance of 1.45 Å from the N-N dimer. Other stable H-I_N complexes contain H or I_N in either a split-interstitial or a tetrahedral configuration, but their binding energies are generally small and in the range of 0.11–0.15 eV.

Figure 6 shows the DOS for TiN with a C atom at a N vacancy site. As for the above case of O atoms at V_N positions, the trapped impurities do not have a large effect on the electronic properties of TiN, at least for the concentrations

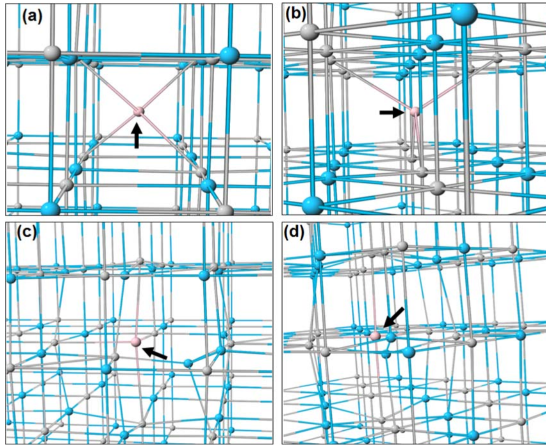

FIG. 7. (Color online) (a) and (b) He tetrahedral interstitial in TiN. (c) and (d) Ar interstitial in TiN. Argon displaces a N atom and occupies its site in the rocksalt structure. The positions of extrinsic species are indicated with arrows. [Ti: gray, N: dark gray (cyan), and He or Ar: light gray (pink) spheres.]

we consider here. However, small features do show up in the DOS even for this low concentration of 3.125%. In particular, the peak on the left side of the DOS valley rises faster and a broad bump (arrow 1 in Fig. 6) is obtained in the energy range of 2.7–3.5 eV below the Fermi level. In contrast, H impurities at V_N do not have a large effect on the electronic properties of TiN and the corresponding DOS (not shown here) shows only a small peak close to the bottom of the valence band. Similarly, the DOS of a TiN crystal with H interstitials in the configurations of Fig. 5(c) resembles the defect-free case in the valley area and the surrounding peaks. However, as shown in Fig. 6, H interstitials do have a distinct DOS signature (arrow 2 in the figure) in the form of a narrow band located at 9 eV below E_F.

C. Inert gas atoms in TiN

Let us now present the results on trapping of noble gas atoms in TiN. The only stable helium interstitial structure is the tetrahedral arrangement depicted in Figs. 7(a) and 7(b). The He atom is at distances of 1.93 and 1.96 Å from the neighboring N and Ti atoms, respectively. Due to its small atomic radius, the interstitial He atom causes a very small distortion on the host TiN crystal. A helium atom is also trapped by a N vacancy with a considerable gain of 1.51 eV in energy. We note that this gain is significantly lower than the corresponding energy gains for the other species above. Conversely, the energy decrease (5.51 eV) that accompanies the release of the He atom of a V_N upon the arrival of a N interstitial is much larger than the corresponding energy gains for O, C, and H. Interstitial He atoms in TiN can form various stable complexes with migrating I_N species. The He-I_N pair with the highest binding energy of 0.57 eV against dissociation comprises a tetrahedral He atom and a vicinal split N interstitial dimer.

In the case of argon in TiN, the trends of trapping and release are qualitatively the same. However, because of the difference in atomic size the quantitative details are markedly different compared to helium. An Ar atom in TiN knocks a N atom out of its crystalline position. The Ar atom takes the position of the N atom and the latter forms a split interstitial with a neighboring N species. The structure is shown in the schematics of Figs. 7(c) and 7(d). The figure also shows clearly the large distortion induced by Ar in the surrounding crystalline matrix. The large stress associated with Ar in TiN can be ameliorated partly when Ar is trapped at a N vacancy site. The trapping of Ar releases then a large amount of 6.37 eV in energy. When a N interstitial arrives in the vicinity of this Ar site it is trapped in the configuration of Fig. 7(c) and the binding energy is 0.65 eV.

A second N interstitial can also be trapped by an Ar atom at a V_N site in TiN. Similar to the above features of Ar trapping, the inert atom in the most stable Ar-I_N pair occupies a crystal site and there are large distortions in its vicinity. The extra N atom appears in a tetrahedral configuration located at 2.25 Å from the Ar site, while a second N interstitial in a split configuration is formed on the other side of the inert gas atom. This defect complex has a binding energy of 0.50 eV against dissociation to isolated Ar and I_N species. Other stable complexes with a binding energy of 0.36 eV comprise vicinal tetrahedral and split I_N species that are located on the same side of a trapped Ar atom in TiN.

Figure 8 illustrates the effect of trapping of He and Ar impurities on the electronic density of states of TiN. Both trapping at N vacancy sites and the extra He and Ar configurations of Fig. 7 are taken into account. The results were obtained using supercells with 32 Ti atoms and 32 or 31 N atoms in the He case, whereas lower concentrations with one impurity per 108 Ti atoms were considered in the case of Ar. In the latter instance, the DOS was scaled to allow comparison with the smaller supercells of 32 Ti atoms. As shown in the figures, the differences of the impurity DOS with respect to the defect-free TiN case are minimal. Interstitial He introduces only a small bump in the DOS around 3 eV below the E_F. In the case of Fig. 7(c), a new peak appears about 8.1 eV below the Fermi level.

IV. LOCAL VIBRATIONAL MODES OF IMPURITIES

The calculations of frequencies for the local vibrational modes around impurities provide a means of identifying the configurations of extrinsic species in TiN. In this section we present the results on local modes calculated through the dynamical matrix of various impurity structures. The results were obtained with supercells of 32 Ti and 32 or 31 N atoms. The active degrees of freedom in the dynamical matrix included the coordinates of the impurities and of neighboring atoms. In particular, seven atoms (the impurity and six nearest Ti neighbors) were included for species trapped at N vacancy sites; while, in the case of interstitial configurations, nine atoms (the impurity and eight nearest Ti and N neighbors) were taken as active in the calculation of local modes.

Raman studies on TiN films[41–47] have revealed a multitude of peaks. For example the typical for TiN films features at about 550–560, 300–320, and 200 $\mathrm{cm^{-1}}$.[41–44] In addition, experiments have recorded peaks in the range of 424–464 $\mathrm{cm^{-1}}$ (Refs. 42–46) and 605–612 $\mathrm{cm^{-1}}$ (Refs.

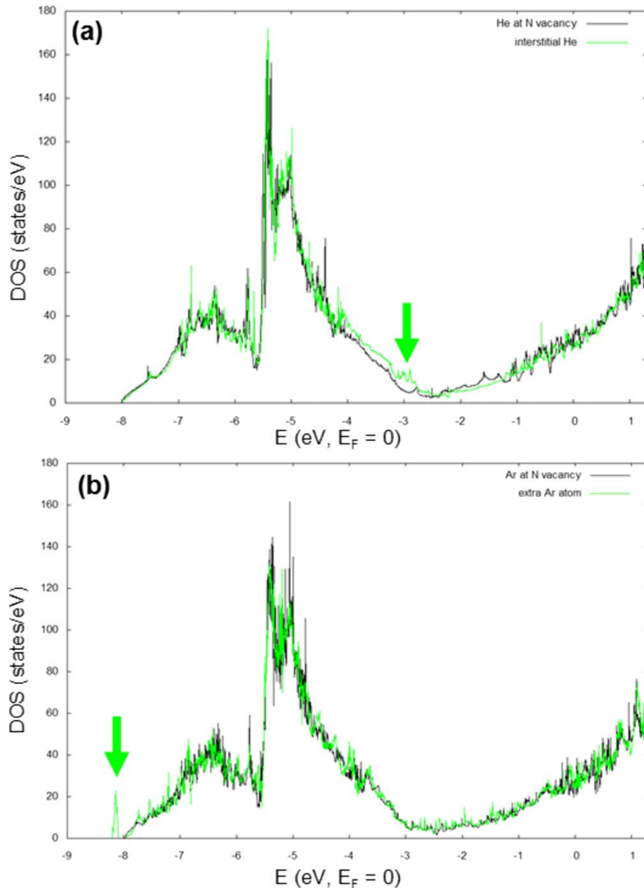

FIG. 8. (Color online) Electronic density of states and effects of trapping of (a) He and (b) Ar in TiN supercells with 32 (108) Ti and 31 (107) or 32 (108) N atoms in the case of He (Ar). Zero of energy is set at the Fermi level. Dark (black) line for impurities at a V_N site and light (green) line for configurations of Figs. 7(a)–7(c). Impurity-related features are shown with arrows. The Ar DOS is scaled to allow comparison with results of the 32 Ti supercells.

42–45), as well as features at 825 cm^{-1} (Ref. 42) and at 1128 cm^{-1} (Ref. 42). Some of these peaks have been interpreted as the results of first- or higher-order Raman scattering; but, to our knowledge, there has been no theoretical study on the origin of observed modes in TiN films.

Starting with results on defect-free TiN, we note that the calculations reproduce the peaks around 550, 310, and 200 cm^{-1} with high accuracy. In particular, the 550 cm^{-1} value corresponds to a calculated (561 cm^{-1}) mode that has a Ti-N-Ti neighboring triplet aligned in the (001) direction and moves as follows: The N atom and one of the Ti atoms move closer to each other, while the second Ti atom move away from the other two atoms. The next calculated mode (308 cm^{-1} corresponds to the simultaneous bending of the two opposite Ti-N-Ti bond pairs on the (001) plane and it can account for the observed 300–320 cm^{-1} peaks. The lowest calculated mode (at 206 cm^{-1}) has the Ti atoms of the (001) and (010) lines moved toward and away from the central N atom, respectively.

For oxygen trapped at a N vacancy site, the highest frequency (422 cm^{-1}) vibration has a Ti-O-Ti triplet moved as in the above case of the 561 cm^{-1} mode of defect-free TiN. The corresponding frequencies for C, H, and Ar are 676, 843, and 488 cm^{-1}, respectively. We note that the O mode is in excellent agreement with the measured modes of 424 cm^{-1} in works[45,46] that studied the evolution of Raman spectra during oxidation of TiN films. Other peaks [at 605 cm^{-1} (Ref. 44) and 612 cm^{-1} (Ref. 45)] that are observed during the oxidation of TiN films could be attributed to the local mode of frequency 614 cm^{-1} for an interstitial O atom [configuration of Fig. 1(c)]. For this vibration, the O atom moves toward one neighboring Ti atom and away from another Ti atom, while it stays almost at the same distance with respect to the remaining two vicinal Ti species.

Other observed modes that are close to calculated frequencies include the 464 and 825 cm^{-1} peaks. The former is very close to a local mode (472 cm^{-1}) for the carbon configuration of Fig. 5(a) and corresponds to movement of the C-N dimer in the (111) direction and toward a neighboring Ti atom. For the latter 825 cm^{-1} peak there are two candidates whose frequency is close to the observed value. One is the highest frequency vibration (810 cm^{-1}) of an interstitial O atom [Fig. 1(c)] and it relates to the stretch of the bond between the impurity and one of its neighboring Ti atoms. The second candidate mode, calculated at 843 cm^{-1}, is the above-mentioned highest frequency mode of a H atom trapped at a N vacancy site.

Finally, let us mention a few calculated high-frequency modes which, although they lack a clear match to available experimental data, might be related to unidentified features of existing multipeak Raman spectra[47] or of future data. First, the highest calculated frequency of the present study corresponds to the stretching mode of the N-H dimer of Fig. 5(c) and has a value of 2816 cm^{-1}. The next mode of the H interstitial is at 1220 cm^{-1} and corresponds to movement of the impurity toward a neighboring (001) plane. Another high-frequency mode at 1227 cm^{-1} relates to the stretching of the C-N dimer of Fig. 5(a). The stretching of an O-N bond of the tetrahedral interstitial configuration of Fig. 1(c) has a frequency of 765 cm^{-1}. Finally, the highest frequency for an Ar atom trapped at N vacancy site is 495 cm^{-1} and relates to a breathing vibration of the surrounding Ti octahedron. We should stress that the measured values depend of course on details of a particular TiN-film-like residual stress fields and concentration of defects.

V. BONDING TOPOLOGY BASED ON THE ELECTRON LOCALIZATION FUNCTION

As impurities move in and out of trapping sites, the possibilities for bonding with surrounding atoms change drastically. In this section, we use the electron localization function[48,49] (ELF) to characterize the types of bonding for different configurations and, in particular, to investigate the conditions that favor the formation of covalent bonds between the extrinsic species and atoms of the TiN matrix. ELF values range from 0 to 1 and the two extremes describe very weak and very strong repulsion, respectively, between two electrons of the same spin. In this context, a covalent bond typically appears in ELF studies as isolated isosurfaces between neighboring atoms and for large ELF values f (nor-

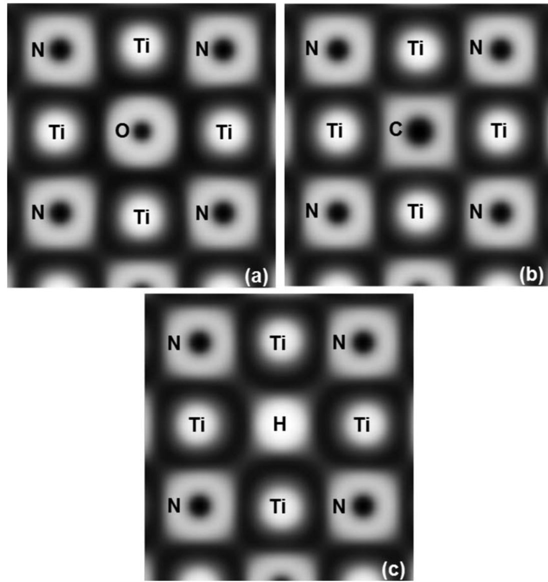

FIG. 9. ELF values f on a (001) plane of TiN with (a) an O, (b) a C, and (c) a H atom trapped at a N vacancy site. The lightest (darkest) areas correspond to $f \approx 0$ ($f \approx 1$) and weak (strong) localization. The absence of the so-called disynaptic basins (such as the ones shown with arrows in Fig. 10) between neighboring valence shells indicate the lack of covalent bonding between the impurities and the neighboring atoms.

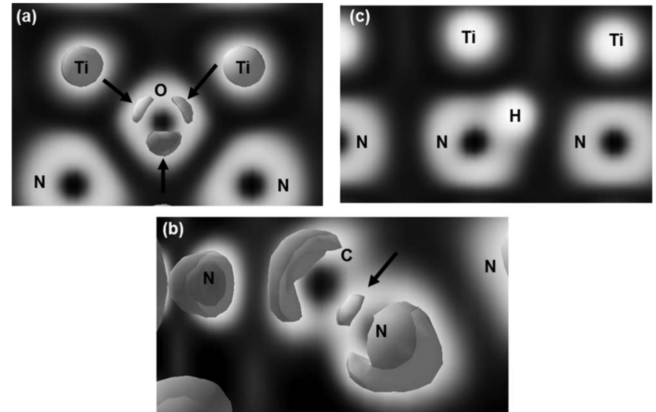

FIG. 10. ELF values f on a (110) plane of TiN with (a) an O [Fig. 1(c)], (b) a C [Fig. 5(a)], and (c) a H [Fig. 5(c)] interstitial atom. The lightest (darkest) areas correspond to $f \approx 0 (f \approx 1)$ and weak (strong) localization. Isosurfaces with $f=0.84 (f=0.78)$ are shown for the O (c) case. The presence of the so-called disynaptic basins (shown with arrows) between neighboring valence shells indicate the formation of covalent bonds between the impurities and neighboring atoms.

mally for $f \geq 0.7$). In the ELF nomenclature these isosurfaces are termed disynaptic. More details on the ELF analysis and terminology can be found in, for example, Refs. 48 and 49.

In Fig. 9 we present the ELF contour plot on a (001) plane of TiN that contains oxygen, carbon, and hydrogen impurities trapped in a nitrogen vacancy site. The results of this section were obtained with Ti PAWs that include the 4s and 3d semicore levels in the valence shell and with supercells of 32 Ti and 32 or 31 N atoms. The energy cutoff was set at 1000 eV and a $8 \times 8 \times 8$ mesh was used for k-point sampling. The detailed analysis of ELF isosurfaces for all possible f values from 0 to 1 reveals that in the cases of Fig. 9 there are no disynaptic ELF basins between the impurities and the surrounding atoms. In addition, the symmetry of the ELF contours around the electronegative impurities resembles the symmetry of the lattice, as is typically found in ELF studies on ionic solids, and shows a high degree of electron localization. The above facts demonstrate that O, C, and H impurities at N vacancy sites do not form covalent bonds with vicinal atoms.

In contrast to trapping at N vacancy sites, the presence of an extra O, C, or H atom in a stoichiometric TiN matrix is characterized by the formation of covalent bonds between the impurity and neighboring atoms. For example, an interstitial O atom [configuration of Fig. 1(c)] forms four bonds with neighboring Ti atoms, bonds that define a tetrahedron as shown in Fig. 10(a). Likewise, a C atom in the configuration of Fig. 5(a) forms a covalent bond with the corresponding displaced N atom, a bond that manifests as the disynaptic basin that is shown with an arrow in the ELF plot of Fig. 10(b). Finally, despite the lack of a disynaptic isosurface, a feature that is typical of H-related ELF studies, the ELF contours for the interstitial H configuration of Fig. 5(c), combined with the fact that the respective N-H distance of 1.06 Å is in the range of typical N-H bond lengths, which point to the formation of a covalent bond between the H impurity and the nearest N atom.

In the case of inert gas atoms such as He and Ar, the ELF analysis shows that there are no covalent bonds between the impurities and the TiN matrix regardless whether the extrinsic species occupy N vacancy sites or appear as extra atoms in a stoichiometric TiN network. In particular, the ELF plots shown in Figs. 11(a)–11(c) demonstrate that the dominant bonding feature is the Pauli repulsion between the impurity and surrounding atoms. Because of this repulsion, the valence shells of vicinal N and Ti atoms show significant distortions especially in the case of trapped Ar and of He interstitial [Figs. 11(b) and 11(c), respectively]. The energetics of He and Ar insertion and, in particular, the strong energetic preference for trapping at N vacancy sites are then controlled by formation of structures, such as the one in Fig. 11(a), for which the Pauli repulsion is minimized.

VI. DISCUSSION

Transition-metal nitrides and carbides have exceptional thermal stability and, in fact, they retain the rocksalt structure even for extreme deviations from the ideal 1:1 stoichiometry. In recent first-principles studies[8,9,39] we showed that N and C vacancies in TiN and TiC remain idle unless the sample is heated to extremely high temperatures. Consequently, once the backbone of the rocksalt structure is formed, the network remains "frozen" even for a high concentration of N or C vacancies. In contrast to vacancies, N interstitials in TiN are significantly more mobile and they can migrate either as isolated species or in pairs.[8,9] These properties of native point defects in TiN are compatible with the presence of a large number of impurities that are trapped

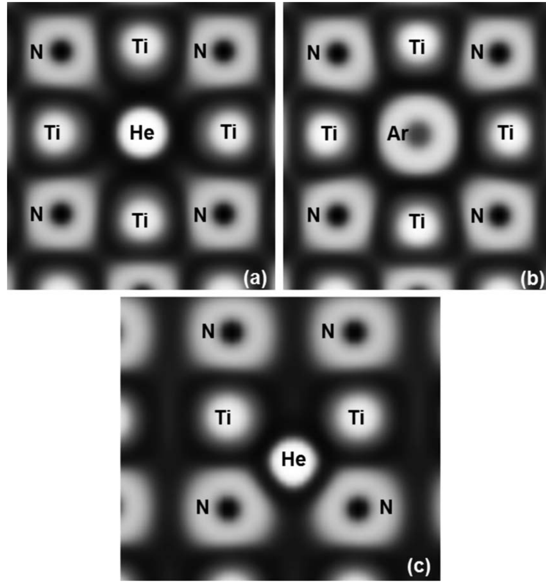

FIG. 11. ELF values f on a (001) plane of TiN with (a) a He and (b) an Ar atom trapped at a N vacancy site. (c) ELF on (110) TiN plane with a He interstitial. The lightest (darkest) areas correspond to $f \approx 0 (f \approx 1)$ and weak (strong) localization. The dominant role of Pauli repulsion between the impurities and neighboring atoms is evident especially for (b) and (c).

either at N vacancies or in complexes with N interstitials. As we noted above, the TiN DOS below the Fermi level shows a peak that relates mostly to N p states. In all the above cases, the impurities disrupt the hybridization of these states by either replacing a N atom with TiN or by forming complexes with N species of the network. For this reason, impurity-induced changes in the DOS appear in the range of the N-p peak. When these changes are strong enough, they can offer means of identifying impurities in TiN through pertinent spectroscopic studies, assuming that the experimental resolution is so high that the impurity peaks can be distinguished from the DOS profile of the host crystal.

The results of this work explain the fundamentals of key processes that are used in the preparation of transition-metal nitride films to control the concentration of impurities. For example, our findings elucidate the atomic-scale physical mechanisms that enable postdeposition nitridation[50] to remove impurities such as oxygen.[18] Specifically, we showed that N interstitials can untrap O, H, and He atoms knocking them out from N vacancy sites. The release of O explains its segregation[28] at grain boundaries of the TiN samples, whereas He release underlies the use of thermal desorption[33] in the study of migration of point defects and its role on thermal stability of TiN.[51]

On the other hand, our results suggest that nitridation alone cannot remove Ar from TiN unless the sample is heated at very high temperatures to allow migration of the Ar-related defect sites of the TiN network. An important effect of nitridation, however, can be the trapping of N around trapped Ar atoms. Because of these possibilities, the compressive stress around Ar atoms in TiN may be either isotropic for isolated Ar at V_N sites or triaxial for stable Ar-I_N complexes. This finding and corresponding results for the other impurities are directly relevant to residual stress studies[52] on TiN.

In the case of carbon, our results point to more complex effects following nitridation of TiN films. Experimental studies[17,18] that employ rapid thermal nitridation (RTN) as post-treatment find that, while carbon impurity levels decrease significantly after RTN, the organometallic carbon concentration does not show equally dramatic changes. Our results are consistent with these findings; indeed, C exchange with migrating N atoms or pairs is not favored. Instead we find that larger defect complexes are formed with C atoms at network sites.

Let us note again that the presence of impurities is important not only because they can modify the physical properties of TiN *per se* but also because they can affect the properties of more complex structures that contain TiN. For example, even 1%–1.5% of oxygen suffices to induce a substantial change[11] in the hardness of TiN/Si_3N_4 nanocomposites, possibly because of segregation of O at the interfacial region. Moreover, O impurities that originate from TiN have been linked[31] to the diffusion barrier properties of TiN/Al/TiN structures employed in copper interconnection of electronic circuits. Finally, hydrogen, whose trapping and release in TiN is detailed in the present work, can play[38,53] a key role on the characteristics of electronic devices including field-effect transistors that employ TiN as metal gates or metal gate coatings.

VII. SUMMARY

In summary, we used first-principles calculations to identify mechanisms of trapping and release of the most common extrinsic species in titanium nitride. All studied species (O, C, H, Ar, and He) are trapped in very stable configurations at nitrogen vacancy sites of TiN. They may then interact with N interstitials and the interaction can lead either to the formation of stable complexes in the case of C and Ar or to the release of O, H, and He to the host crystal. We showed that in certain cases, even low impurity levels can have discernible effects on the properties of TiN inducing peaks in the electronic density of states. We also demonstrated that impurity-related modes can explain observed features of vibrational spectra and we analyzed the character of bonding around trapped impurities.

ACKNOWLEDGMENTS

The authors acknowledge the support by the McMinn Endowment at Vanderbilt University, AFOSR MURI under Grant No. FA9550-05-1-0306 and by the Greek Secretariat of Research and Technology under Grant No. ΠENEΔ-03EΔ613. The calculations were performed at ORNL Center for Computational Sciences.

[1] L. Hultman, Vacuum **57**, 1 (2000).
[2] I. Pollini, A. Mosser, and J. C. Parlebas, Phys. Rep. **355**, 1 (2001).
[3] H. Höchst, R. D. Bringans, P. Steiner, and T. Wolf, Phys. Rev. B **25**, 7183 (1982).
[4] A. J. Perry, J. Vac. Sci. Technol. A **6**, 2140 (1988).
[5] S. H. Jhi, J. Ihm, S. G. Louie, and M. L. Cohen, Nature (London) **399**, 132 (1999).
[6] D. J. Kim, Y. B. Jung, M. B. Lee, Y. H. Lee, J. H. Lee, and J. H. Lee, Thin Solid Films **372**, 276 (2000).
[7] C. S. Shin, D. Gall, N. Hellgren, J. Patscheider, I. Petrov, and J. E. Greene, J. Appl. Phys. **93**, 6025 (2003).
[8] L. Tsetseris, N. Kalfagiannis, S. Logothetidis, and S. T. Pantelides, Phys. Rev. Lett. **99**, 125503 (2007).
[9] L. Tsetseris, N. Kalfagiannis, S. Logothetidis, and S. T. Pantelides, Phys. Rev. B **76**, 224107 (2007).
[10] J. Musil, Surf. Coat. Technol. **125**, 322 (2000).
[11] S. Veprek, H. D. Mannling, A. Niederhofer, D. Ma, and S. Mukherjee, J. Vac. Sci. Technol. B **22**, L5 (2004).
[12] S. Hao, B. Delley, S. Veprek, and C. Stampfl, Phys. Rev. Lett. **97**, 086102 (2006).
[13] S. W. Wang, R. Gudipati, A. S. Rao, T. J. Bostelmann, and Y. G. Shen, Appl. Phys. Lett. **91**, 081916 (2007).
[14] I. Petrov, L. Hultman, J. L. Sundgren, and J. E. Greene, J. Vac. Sci. Technol. A **10**, 265 (1992).
[15] W. Ensinger and K. Volz, Mater. Sci. Eng., A **253**, 234 (1998).
[16] R. Fix, R. G. Gordon, and D. M. Hoffman, Chem. Mater. **3**, 1138 (1991).
[17] M. Danek, M. Liao, J. Tseng, K. Littau, D. Saigal, H. Zhang, R. Mosely, and M. Eizenberg, Appl. Phys. Lett. **68**, 1015 (1996).
[18] J. H. Yun, E. S. Choi, C. M. Jang, and C. S. Lee, Jpn. J. Appl. Phys., Part 2 **41**, L418 (2002).
[19] M. Juppo, P. Alen, M. Ritala, T. Sajavaara, J. Keinonen, and M. Leskela, Electrochem. Solid-State Lett. **5**, C4 (2002).
[20] J. Probst, U. Gbureck, and R. Thull, Surf. Coat. Technol. **148**, 226 (2001).
[21] J. S. Min, Y. W. Son, W. G. Kang, S. S. Chun, and S. W. Kang, Jpn. J. Appl. Phys., Part 1 **37**, 4999 (1998).
[22] J. Y. Kim, D. Y. Kim, H. O. Park, and H. T. Jeon, J. Electrochem. Soc. **152**, G29 (2005).
[23] D. M. Hoffman, Polyhedron **13**, 1169 (1994).
[24] M. Ritala, T. Asikainen, M. Leskela, J. Joikinen, R. Lappalainen, M. Utriainen, L. Niinisto, and E. Ristolainen, Appl. Surf. Sci. **120**, 199 (1997).
[25] M. Ritala, M. Leskela, E. Rauhala, and J. Jokinen, J. Electrochem. Soc. **145**, 2914 (1998).
[26] E. K. Evangelou, N. Konofaos, X. A. Aslanoglou, C. A. Dimitriadis, P. Patsalas, S. Logothetidis, M. Kokkoris, E. Kossionides, R. Vlastou, and R. Groetschel, J. Appl. Phys. **88**, 7192 (2000).
[27] M. Nose, M. Zhou, E. Honbo, M. Yokota, and S. Saji, Surf. Coat. Technol. **142-144**, 211 (2001).
[28] R. Kroger, M. Eizenberg, C. Marcadal, and L. Chen, J. Appl. Phys. **91**, 5149 (2002).
[29] E. Alves, A. R. Ramos, N. P. Barradas, F. Vaz, P. Cerqueira, L. Rebouta, and U. Kreissig, Surf. Coat. Technol. **180-181**, 372 (2004).
[30] F. Vaz, P. Cerqueira, L. Rebouta, S. M. C. Nascimento, E. Alves, P. Goudeau, J. R. Riviere, K. Pischow, and J. de Rijk, Thin Solid Films **447-448**, 449 (2004).
[31] Y. H. Shin and Y. Shimogaki, Sci. Technol. Adv. Mater. **5**, 399 (2004).
[32] L. M. Liu, S. Q. Wang, and H. Q. Ye, J. Phys.: Condens. Matter **17**, 5335 (2005).
[33] W. H. B. Hoondert, B. J. Thijsse, and A. van den Beukel, Surf. Coat. Technol. **66**, 472 (1994).
[34] J. P. Perdew and Y. Wang, Phys. Rev. B **45**, 13244 (1992).
[35] P. E. Blöchl, Phys. Rev. B **50**, 17953 (1994).
[36] G. Kresse and D. Joubert, Phys. Rev. B **59**, 1758 (1999).
[37] D. J. Chadi and M. L. Cohen, Phys. Rev. B **8**, 5747 (1973).
[38] L. Tsetseris, D. M. Fleetwood, R. D. Schrimpf, X. J. Zhou, I. G. Batyrev, and S. T. Pantelides, Microelectron. Eng. **84**, 2344 (2007).
[39] L. Tsetseris and S. T. Pantelides, Acta Mater. **56**, 2864 (2008).
[40] O. Jepson and O. K. Andersen, Solid State Commun. **9**, 1763 (1971).
[41] R. Chowdhury, R. D. Vispute, K. Jagannadham, and J. Narayan, J. Mater. Res. **11**, 1458 (1996).
[42] C. P. Constable, J. Yarwood, and W. D. Münz, Surf. Coat. Technol. **116-119**, 155 (1999).
[43] S. Logothetidis, E. I. Meletis, and G. Kourouklis, J. Mater. Res. **14**, 436 (1999).
[44] H. C. Barshilia and K. S. Rajam, J. Mater. Res. **19**, 3196 (2004).
[45] S. M. Oh and T. Ishigaki, Thin Solid Films **457**, 186 (2004).
[46] P. W. Shum, K. Y. Li, Z. F. Zhou, and Y. G. Shen, Surf. Coat. Technol. **185**, 245 (2004).
[47] R. Subramanian and M. Jayachandran, J. Appl. Electrochem. **37**, 1069 (2007).
[48] B. Silvi and A. Savin, Nature (London) **371**, 683 (1994).
[49] B. Silvi and C. Gatti, J. Phys. Chem. A **104**, 947 (2000).
[50] H. Kim, J. Vac. Sci. Technol. B **21**, 2231 (2003).
[51] G. Abadias, Y. Y. Tse, P. Guérin, and V. Pelosin, J. Appl. Phys. **99**, 113519 (2006).
[52] J. D. Kamminga, T. H. de Keijser, R. Delhez, and E. J. Mittemeijer, J. Appl. Phys. **88**, 6332 (2000).
[53] S. T. Pantelides, L. Tsetseris, S. N. Rashkeev, X. J. Zhou, D. M. Fleetwood, and R. D. Schrimpf, Microelectron. Reliab. **47**, 903 (2007).